Accurate, efficient, and (iso)geometrically flexible collocation methods for phase-field models

Hector Gomez[a], Alessandro Reali[b,*], Giancarlo Sangalli[c]

[a]*University of A Coruña, Department of Mathematical Methods, Campus de Elviña, s/n, 15192, A Coruña, Spain*
[b]*University of Pavia, Department of Civil Engineering and Architecture, via Ferrata 3, 27100, Pavia, Italy*
[c]*University of Pavia, Dipartimento di Matematica "F. Casorati", via Ferrata, 1, 27100, Pavia, Italy*

Abstract

We propose new collocation methods for phase-field models. Our algorithms are based on Isogeometric Analysis, a new technology that makes use of functions from computational geometry, such as, for example, Non-Uniform Rational B-Splines (NURBS). NURBS exhibit excellent approximability and controllable global smoothness, and can represent exactly most geometries encapsulated in Computer Aided Design (CAD) models. These attributes permitted us to derive accurate, efficient, and geometrically flexible collocation methods for phase-field models. The performance of our method is demonstrated by several numerical examples of phase separation modeled by the Cahn-Hilliard equation. We feel that our method successfully combines the geometrical flexibility of finite elements with the accuracy and simplicity of pseudo-spectral collocation methods, and is a viable alternative to classical collocation methods.

Key words: Collocation, Cahn-Hilliard equation, NURBS, Isogeometric analysis, Phase-field models

1. Introduction

The Cahn-Hilliard equation is a central model in nonlinear interface dynamics [5] and pattern formation [63]. It was derived about fifty years ago as a model for phase separation of immiscible fluids [23, 24]. Since then, it has been applied to a variety of physical problems, including planet formation [70], microstructure evolution of binary mixtures [2, 3, 26] and phase separation of polymer blends [27]. The Cahn-Hilliard equation is also one of the simplest equations that can model stable co-existence of two phases and, as such, is the basis for various multiphase flow theories [31, 32, 57, 60]. Even more important is the fact that the ideas behind the Cahn-Hilliard equation have given rise to a new class of mathematical models termed phase-field models [39]. These models treat the interfaces as diffuse, track their dynamical evolution, and encode the interfacial physics at once. Phase-field models have had a significant impact on condensed matter physics [36, 37], fluid mechanics [16, 44], and solid mechanics [20, 61, 62]. Since the numerical challenges faced when dealing with phase-field equations are common to many different models, we feel that studying efficient and accurate algorithms for the Cahn-Hilliard equation is a significant goal in computational physics.

The Cahn-Hilliard model is a nonlinear partial differential equation that involves fourth-order derivatives in space. Typical solutions to the equation include thin layers that evolve dynamically through the computational domain. The length scale of these layers is given by a small parameter that multiplies the fourth-order derivative, making the problem singularly perturbed. All these features make the numerical approximation of

the Cahn-Hilliard equation a significant challenge. Although, new finite element methods are being proposed to solve the Cahn-Hilliard equation [43, 68, 72], collocation methods continue to be the standard methodology for computational phase field modeling. The two most representative examples of collocation methods for phase field models are the finite difference method [12, 25, 50, 67] and spectral methods [12, 33, 52, 66, 69].

5   Most work on collocation methods for the Cahn-Hilliard equation has been focused on the development of algorithms to study the structure of the spatial patterns and free-energy evolution in extended systems, like in the spirit of the problem of isotropic turbulence decay in fluid mechanics. It is, however, becoming clear that technological applications will demand accurate and robust algorithms that can handle complicated geometries and boundary conditions (a significant example has been recently presented in [4]). This paper
10   constitutes a first step in this direction. We propose a new collocation method for the Cahn-Hilliard equation that is fast, accurate, robust, geometrically flexible, and can handle a variety of different boundary conditions.

Our collocation scheme is based on Isogeometric Analysis (IGA) [28, 55]. IGA is a computational technology that uses functions from computational geometry to represent both the solution and the domain of a boundary-value problem. The most frequently utilized functions are Non-Uniform Rational B-Splines
15   (NURBS) [29, 55] and T-Splines [13] which are widely used in computational geometry and design. The first applications of IGA were within the framework of finite element discretizations in which NURBS replaced the standard piece-wise polynomials, giving rise to new and more accurate discretizations on a per-degree-of-freedom basis [10, 14, 15, 21, 22, 30, 34, 38, 48, 56, 58, 59, 64]. In fact, IGA is a generalization of finite elements because NURBS are a superset of piece-wise polynomials. However, IGA offers new possibilities
20   not available in classical finite elements [54], such as, for example, the straightforward generation of basis functions of arbitrarily high global smoothness. Within the context of geometrically flexible methods, this seems to be a unique attribute of IGA with profound implications on the accuracy of the discretization [1, 17, 29, 41]. Additionally, the possibility of generating arbitrarily smooth basis functions on complicated domains opens the door to geometrically flexible collocation methods [8], which have been already success-
25   fully applied in the fields of elastostatics and explicit elastodynamics [9], as well as for the development of innovative structural elements [11, 18]. A detailed study on the advantages of isogeometric collocation over Galerkin approaches is provided by [65]. In that paper, the authors show the superior behavior, in terms of accuracy-to-computational-time ratio, attained by collocation with respect to Galerkin, in particular for higher order approximations; moreover, they introduce and analyze adaptive isogeometric collocation
30   methods based on local hierarchical refinement of NURBS.

Here we use these ideas to derive new collocation methods for phase-field models. The numerical examples in this paper show that our algorithms are very efficient, and seem to be a successful combination of the geometrical flexibility of classical finite element methods and the accuracy, efficiency, and simplicity of pseudo-spectral collocation methods.

35   The outline of this paper is as follows: We introduce the Cahn-Hilliard equation in Section 2. Our numerical formulation is presented in Section 3. Section 4 illustrates, with several numerical examples, the efficiency, accuracy, and geometrical flexibility of our algorithm. We draw conclusion in Section 5.

2. The Cahn-Hilliard equation

We present the Cahn-Hilliard equation in the context of isotropic and isothermal phase separation of immiscible fluids. Within this simplified setting, the thermodynamic state of the mixture is defined by an order parameter u of the mass fraction. The assumption of an isothermal system indicates that the relevant thermodynamic potential is a free energy, which in the context of two-phase immiscible mixtures is called Ginzburg-Landau free energy.

2.1. Ginzburg-Landau free energy

Let V be an open subset of $\mathbb{R}^d$, where d is the spatial dimension. The Ginzburg-Landau free energy is defined as the functional $\mathcal{G} : H^1(V) \mapsto \mathbb{R}$ which takes the form

$$\mathcal{G}[u] = \int_V \left(F(u) + \frac{\varepsilon^2}{2} |\nabla u|^2 \right) \mathrm{d}V \tag{1}$$

where H^1 is the Sobolev space of square integrable functions with square integrable first derivatives. Following the interpretation of Cahn and Hilliard [23, 24], F is the free energy of an homogeneous system and the gradient term accounts for the interfacial free energy. Among the various possibilities for the homogeneous free energy F, we take the simple form

$$F(u) = \frac{\alpha}{4} \left(u^2 - \frac{\beta}{\alpha} \right)^2 \tag{2}$$

This function is non-convex and presents a double well structure with two local minima located at $u = -\sqrt{\beta/\alpha}$ and $u = +\sqrt{\beta/\alpha}$, which are called the binodal points.

The Cahn-Hilliard equation is a statement of mass conservation

$$\frac{\partial u}{\partial t} + \nabla \cdot \boldsymbol{j} = 0 \tag{3}$$

where the mass flux $\boldsymbol{j}$ is chosen such that the Ginzburg-Landau free energy decreases with time. This can be achieved taking

$$\boldsymbol{j} = -\nabla \left(\frac{\delta \mathcal{G}}{\delta u} \right) \tag{4}$$

where $\delta\mathcal{G}/\delta u$ represents the variational derivative of $\mathcal{G}$ with respect to variations of u that vanish on ∂V. Using Eqs. (3) and (4) we obtain the Cahn-Hilliard equation

$$\frac{\partial u}{\partial t} = \Delta \left(f(u) - \varepsilon^2 \Delta u \right) \tag{5}$$

where

$$f(u) = F'(u) = \alpha u^3 - \beta u \tag{6}$$

is the chemical potential of a uniform solution. For an alternative derivation based on a microforce balance, the reader is referred to [51].

Since the dynamics of the Cahn-Hilliard equation is driven by the minimization of the Ginzburg-Landau free energy, the solution will approach the binodal points, defining a spatial structure with patches of each of

the phases that dynamically coarsen over time. The patches of pure phases are separated by thin layers with thickness ν. A typical argument to find how ν scales with the physical parameters of the model is to obtain a one-dimensional, stationary solution to the Cahn-Hilliard equation on an infinite domain. That solution should represent a fully separated flow. This can be achieved by solving the ordinary differential equation $\alpha u_s^3 - \beta u_s - \varepsilon^2 u_s'' = 0$ in $x \in (-\infty, +\infty)$ subject to boundary conditions $u_s(\pm\infty) = \pm\sqrt{\beta/\alpha}$. The solution of the last equation is $u_s(x) = \sqrt{\beta/\alpha} \tanh\left(\sqrt{\beta/2}\, x/\varepsilon\right)$ which, for fixed β, indicates that $\nu \sim \varepsilon$. Based on this result, we proposed in [43] an argument to select the mesh characteristic length of a numerical scheme in terms of ε.

2.2. Initial/boundary-value problem

Let us assume that the spatial domain V has a smooth boundary ∂V that can be decomposed into two complementary parts as $\partial V = \overline{\partial V_D \cup \partial V_N}$. We state the following initial/boundary-value problem over the spatial domain V and the time interval $(0, T)$: given $u_0 : \overline{V} \mapsto \mathbb{R}$ and $u_D : \partial V_D \mapsto \mathbb{R}$, find $u : \overline{V} \times [0, T] \mapsto \mathbb{R}$ such that

$$\frac{\partial u}{\partial t} = \Delta \left(f(u) - \varepsilon^2 \Delta u\right) \qquad \text{in} \quad V \times (0, T) \tag{7}$$

$$u = u_D \qquad \text{on} \quad \partial V_D \times [0, T] \tag{8}$$

$$\nabla \left(f(u) - \varepsilon^2 \Delta u\right) \cdot \boldsymbol{n} = 0 \qquad \text{on} \quad \partial V_N \times [0, T] \tag{9}$$

$$\nabla u \cdot \boldsymbol{n} = 0 \qquad \text{on} \quad \partial V \times [0, T] \tag{10}$$

$$u(\boldsymbol{x}, 0) = u_0(\boldsymbol{x}) \qquad \text{in} \quad \overline{V} \tag{11}$$

3. Numerical formulation

Here we present our fully discrete algorithm for the Cahn-Hilliard equation. We start by defining a time-discrete version of the equation, which is eventually discretized in space using our isogeometric collocation methods.

3.1. Time discretization

We utilize the linearly stabilized Eyre's method [40] to perform time integration. Thus, the non-convex homogeneous free energy F is split into two convex functions F_c and F_e, as follows,

$$F(u) = F_c(u) - F_e(u) \tag{12}$$

We call F_c and F_e the contractive and expansive parts because they reduce and increase, respectively, the $\mathcal{L}^2$ energy into the system. This splitting is always possible, but it is not unique. Among the various possibilities, we take

$$F_c(u) = \beta u^2, \quad F_e(u) = -\frac{\alpha}{4} u^4 + 3\frac{\beta}{2} u^2 + \frac{\alpha\beta^2}{4\alpha^2} \tag{13}$$

4

which satisfies the necessary requirements, namely, the functions F_c and F_e are both convex in the physically relevant domain and they verify equation (12). The chemical potentials associated to this splitting are given by,

$$f_c(u) = 2\beta u, \quad f_e(u) = -\alpha u^3 + 3\beta u \tag{14}$$

In what follows, we present our time-stepping scheme. Let us divide the time interval of interest $[0, T]$ into N subintervals (t_n, t_{n+1}); $n = 0, \ldots, N-1$, where $t_0 = 0$ and $t_N = T$. We use the notation $\delta_n = t_{n+1} - t_n$. We call u_n the time discrete approximation to $u(t_n)$, where we have omitted the dependence on the spatial coordinate for simplicity. We propose the following time integration algorithm: Given u_n, find u_{n+1} such that

$$\frac{u_{n+1} - u_n}{\delta_n} = \Delta \left(f_c(u_{n+1}) - f_e(u_n) - \varepsilon^2 \Delta u_{n+1} \right) \tag{15}$$

Equation (15) may be rewritten as

$$u_{n+1} - 2\beta \delta_n \Delta u_{n+1} + \varepsilon^2 \delta_n \Delta^2 u_{n+1} = u_n + 6\alpha \delta_n u_n |\nabla u_n|^2 + 3\delta_n (\alpha u_n^2 - \beta) \Delta u_n \tag{16}$$

We note that the algorithm (16) is linearly implicit and, thus, the updates can be computed every time step by solving a linear problem. Although the unconditional stability of this method is out of the scope of this paper, we note that this method has been shown to be unconditionally stable when combined with certain spatial discretizations (for a detailed discussion on unconditionally stable schemes for the Cahn-Hilliard equation, the reader is referred to [45] or [35, 42, 46, 47, 49, 52, 53]). In our case, we expect the algorithm to at least permit taking time steps significantly larger than those employed by explicit methods.

3.2. Space discretization

Our space discretization makes use of the finite-dimensional spaces generated by Non-Uniform Rational B-Splines (NURBS), which, in turn, originate from B-Splines. Thus, we start our presentation showing how to generate a B-Spline basis.

3.2.1. One-dimensional B-Splines

A one-dimensional B-Spline basis is a set of n piecewise polynomial functions of degree p denoted by $\{B_{i,p}\}_{i=1,\ldots,n}$. These functions are generated from a knot vector, which is a set of non-decreasing coordinates (in parametric space) called knots. Let us introduce the following *knot vector*

$$\boldsymbol{K}_\xi = (\xi_1, \xi_2, \ldots, \xi_{n+p+1}). \tag{17}$$

Without loss of generality, it may be assumed that $\xi_1 = 0$ and $\xi_{n+p+1} = 1$, and the basis functions are defined on the interval $[0, 1]$. Moreover, we assume that the knot vector is *open*, that is, $\xi_1 = \ldots = \xi_{p+1}$ and $\xi_{n+1} = \ldots = \xi_{n+p+1}$. Given p and $\boldsymbol{K}_\xi$, we define the zeroth degree B-Spline functions $\{B_{i,0}\}_{i=1,\ldots,n}$ as

$$B_{i,0}(\xi) = \begin{cases} 1 & \text{if} \quad \xi_i \leq \xi < \xi_{i+1} \\ 0 & \text{otherwise} \end{cases} \tag{18}$$

The p-th degree B-Splines basis functions are defined recursively using the relation

$$B_{i,q}(\xi) = \frac{\xi - \xi_i}{\xi_{i+p} - \xi_i} B_{i,q-1}(\xi) + \frac{\xi_{i+p+1} - \xi}{\xi_{i+p+1} - \xi_{i+1}} B_{i+1,q-1}(\xi); \quad i = 1, \ldots, n; \quad q = 1, \ldots, p. \tag{19}$$

The functions $\{B_{i,p}\}_{i=1,\ldots,n}$ are $\mathcal{C}^\infty$ everywhere except at the knots. At a non-repeated knot, the functions have $p - 1$ continuous derivatives. If a knot has multiplicity k, the number of continuous derivatives at that point is $p - k$.

3.2.2. Two-dimensional B-Splines

Given two polynomial degrees $p^{(i)}$, $i = 1, 2$ and two knot vectors $\boldsymbol{K}_\gamma$, $\gamma = \xi^{(1)}, \xi^{(2)}$ of lengths $n^{(i)} + p^{(i)} + 1$, respectively, two-dimensional B-Spline functions are defined by taking tensor products of their one-dimensional counterparts

$$B_{i^{(1)},i^{(2)}}(\xi^{(1)}, \xi^{(2)}) = \otimes_{\gamma=1}^2 B_{i^{(\gamma)},p^{(\gamma)}}(\xi^{(\gamma)}) \tag{20}$$

We will denote Ξ the parametric space, which may be assumed to be $\Xi = [0,1]^2$. Using the functions (20) we can generate a volumetric object $V = \boldsymbol{F}_B(\boldsymbol{\xi})$ by way of the geometrical map $\boldsymbol{F}_B$ such that

$$\boldsymbol{F}_B(\boldsymbol{\xi}) = \sum_{i \in I} \boldsymbol{C}_i B_i(\boldsymbol{\xi}) \quad \forall \boldsymbol{\xi} \in \Xi \tag{21}$$

where $\boldsymbol{C}_i \in \mathbb{R}^2$ are the control points and

$$I = \{\boldsymbol{i} = (i^{(1)}, i^{(2)}) \in \mathbb{N}^2, \ i^{(k)} = 1, \ldots, n^{(k)} + p^{(k)} + 1\} \tag{22}$$

3.2.3. Non-Uniform Rational B-Splines (NURBS)

NURBS geometrical objects in $\mathbb{R}^d$ are projective transformations of B-Spline geometrical entities in $\mathbb{R}^{d+1}$. Let $\widehat{\boldsymbol{C}}_i \in \mathbb{R}^2$ be a set of control points in two-dimensional space and ω_i a set of positive real numbers called weights such that $(\widehat{\boldsymbol{C}}_i, w_i) \in \mathbb{R}^3$. We define the following B-Spline geometrical object in $\mathbb{R}^3$ as,

$$\widehat{V} = \widehat{\boldsymbol{F}}(\Xi) \tag{23}$$

where

$$\widehat{\boldsymbol{F}}(\boldsymbol{\xi}) = \sum_{i \in I} (\widehat{\boldsymbol{C}}_i, w_i) B_i(\boldsymbol{\xi}), \quad \boldsymbol{\xi} \in \Xi \tag{24}$$

The NURBS object V is defined as

$$V = \boldsymbol{F}(\Xi) \tag{25}$$

where the geometrical mapping $\boldsymbol{F}$ is defined as,

$$\boldsymbol{F}(\boldsymbol{\xi}) = \sum_{i \in I} \frac{\widehat{\boldsymbol{C}}_i}{w_i} \frac{w_i B_i(\xi)}{\sum_{j \in I} w_j B_j(\xi)}, \quad \boldsymbol{\xi} \in \Xi \tag{26}$$

Denoting,

$$\overline{\boldsymbol{C}}_i = \frac{\widehat{\boldsymbol{C}}_i}{w_i}, \quad W(\boldsymbol{\xi}) = \sum_{i \in I} w_i B_i(\boldsymbol{\xi}), \quad R_i(\boldsymbol{\xi}) = \frac{w_i B_i(\boldsymbol{\xi})}{W(\xi)} \tag{27}$$

we have that

$$\boldsymbol{F}(\boldsymbol{\xi}) = \sum_{i \in I} \overline{\boldsymbol{C}}_i R_i(\boldsymbol{\xi}), \quad \boldsymbol{\xi} \in \Xi \tag{28}$$

We will call R_i, $\boldsymbol{i} \in I$, NURBS basis functions in parametric space.

6

3.2.4. Discrete space

NURBS basis functions in physical space are defined as the push forward of the functions $R_{\boldsymbol{i}}$, $\boldsymbol{i} \in I$. The discrete space that we will use for our numerical method is the space spanned by those functions, namely

$$\mathcal{V}^h = \mathrm{span}\{R_{\boldsymbol{i}} \circ \boldsymbol{F}^{-1}, \ \boldsymbol{i} \in I\} \tag{29}$$

where the superscript h denotes the mesh-size and also indicates that $\mathcal{V}^h$ is a finite-dimensional discrete space. Approximation properties of $\mathcal{V}^h$ depend on the mesh-size: we refer to [19] for the mathematical details.

3.2.5. Collocation strategy

In order to motivate our collocation scheme for the spatial discretization, we first discuss the one-dimensional fourth-order toy problem

$$\frac{\partial^4}{\partial \xi^4} \phi(\xi) = g(\xi), \quad \forall \xi \in (0,1) \tag{30}$$

$$\frac{\partial}{\partial \xi} \phi(0) = \frac{\partial}{\partial \xi} \phi(1) = 0 \tag{31}$$

$$\frac{\partial^3}{\partial^3 \xi} \phi(0) = \frac{\partial^3}{\partial^3 \xi} \phi(1) = 0 \tag{32}$$

where g is a continuous funtion on $(0,1)$ and ϕ is the unknown. Assume that we look for an approximate solution $\phi^h \in \mathrm{span}\{B_{i,p}\}_{i=1,\dots,n}$, that is, a degree p, dimension n, spline on a given knot vector. It is understood that the spline regularity is at least C^4 and therefore the degree is $p > 4$. Because of the boundary conditions (31)-(32) that account for 4 independent equations, we have to derive $n - 4$ equations from (30). In the collocation setting, we need to introduce collocation points, denoted $\hat{\tau}_j$, for $j = 3, \dots, n-2$, and set

$$\frac{\partial^4}{\partial \xi^4} \phi^h(\hat{\tau}_j) = g(\hat{\tau}_j), \quad \forall j = 3, \dots, n-2. \tag{33}$$

Notice that (33) are indeed $n - 4$ equations, and with the two boundary conditions at 0 (which can be associated to $j = 1, 2$) and at 1 (which can be associated to $j = n - 1, n$) we have a square linear system. Notice also that (33) is an interpolation problem on fourth-order derivative of splines, that is, for splines of degree $p - 4$ on the same knot vector. A natural choice is then to select suitable interpolation points for the space $\mathrm{span}\{B_{i,p-4}\}_{i=3,\dots,n-2}$ as $\hat{\tau}_j$. One possibility is then to select *Greville sites* for degree $p - 4$ splines, that is,

$$\hat{\tau}_j = \frac{1}{p-4} \sum_{i=j+3}^{j+p-2} \xi_i \tag{34}$$

Observe that, from the open knot vector property, the first and last collocation points above are the interval endpoints, that is $\hat{\tau}_3 = 0$ and $\hat{\tau}_{n-2} = 1$.

If the differential operator included lower-order terms (e.g., second-order derivatives or zero-order terms as in Eq. (16)), then (34) would still be a valid choice. Indeed, following e.g. the argument of [8], one can prove the convergence of such a scheme under suitable assumptions.

7

For the time-discrete Cahn-Hilliard equation in two dimensions, the problem to be addressed is (16). Assuming that the right-hand side of Eq. (16) is known, we look for u such that

$$u - a\Delta u + b\Delta^2 u = r \quad \text{in } V \tag{35}$$

$$\nabla u \cdot \boldsymbol{n} = 0 \quad \text{on } \partial V \tag{36}$$

$$\nabla(\Delta u) \cdot \boldsymbol{n} = 0 \quad \text{on } \partial V \tag{37}$$

with $a = 2\beta\delta_n$ and $b = \varepsilon^2\delta_n$, and where we have considered the Neumann boundary condition (10) and, accordingly, we have simplified the flux condition (9). Note that we have also assumed $V_D = \emptyset$. The two-dimensional collocation scheme for (35)–(37) can be designed in the lines of the one-dimensional scheme above. First, we look for a discrete solution u^h in the space $\mathcal{V}^h$ defined in (29), which has dimension

$$\dim(\mathcal{V}^h) = n^{(1)}n^{(2)} \tag{38}$$

Then, we set the collocation points on the parametric domain as the tensor product of (34), that is

$$\hat{\boldsymbol{\tau}}_\nu^C = \left(\frac{1}{p^{(1)} - 4} \sum_{i=j^{(1)}+3}^{j^{(1)}+p^{(1)}-2} \xi_i^{(1)}, \frac{1}{p^{(2)} - 4} \sum_{i=j^{(2)}+3}^{j^{(2)}+p^{(2)}-2} \xi_i^{(2)} \right), \quad \nu \equiv (j^{(1)}, j^{(2)}) \in \mathcal{I}^C \tag{39}$$

where the index set is

$$\mathcal{I}^C = \{3, \ldots, n^{(1)} - 2\} \times \{3, \ldots, n^{(2)} - 2\}$$

The collocation points (39) for a particular example can be observed in Figure 1. If the computational domain is a mapped geometry V, the collocation points on V are the push-forward of (39)

$$\boldsymbol{\tau}_\nu^C = \boldsymbol{F}(\hat{\boldsymbol{\tau}}_\nu^C) \tag{40}$$

where $\boldsymbol{F}$ is the NURBS mapping defined in Eq. (26). Finally, we collocate equation (35) as

$$u^h(\boldsymbol{\tau}_\nu^C) - a\Delta u^h(\boldsymbol{\tau}_\nu^C) + b\Delta^2 u^h(\boldsymbol{\tau}_\nu^C) = r(\boldsymbol{\tau}_\nu^C), \quad \forall\nu \in \mathcal{I}^C \tag{41}$$

Boundary conditions as (36) and (37), or of more general kind, can be imposed by interpolation. For this purpose, we introduce on the boundary of the parametric domain $[0,1]^2$ the Greville sites for degree p splines, that is

$$
\begin{aligned}
\left\{ \hat{\boldsymbol{\tau}}_\nu^{BC}, \quad \nu \in \mathcal{I}^{BC} \right\} = &\left\{ \left(\frac{1}{p^{(1)}} \sum_{i=j^{(1)}+1}^{j^{(1)}+p^{(1)}} \xi_i^{(1)}, 0 \right), \quad j^{(1)} \in \{1, \ldots, n^{(1)}\} \right\} \\
\cup &\left\{ \left(\frac{1}{p^{(1)}} \sum_{i=j^{(1)}+1}^{j^{(1)}+p^{(1)}} \xi_i^{(1)}, 1 \right), \quad j^{(1)} \in \{1, \ldots, n^{(1)}\} \right\} \\
\cup &\left\{ \left(0, \frac{1}{p^{(2)}} \sum_{i=j^{(2)}+1}^{j^{(2)}+p^{(2)}} \xi_i^{(2)} \right), \quad j^{(2)} \in \{2, \ldots, n^{(2)} - 1\} \right\} \\
\cup &\left\{ \left(1, \frac{1}{p^{(2)}} \sum_{i=j^{(2)}+1}^{j^{(2)}+p^{(2)}} \xi_i^{(2)} \right), \quad j^{(2)} \in \{2, \ldots, n^{(2)} - 1\} \right\}
\end{aligned} \tag{42}
$$

where the first two line sets refer to the $2n^{(1)}$ points on the two horizontal edges of $[0,1]^2$, and include the four corners, while the third and fourth line sets refer to the $2n^{(2)} - 4$ points on the two vertical edges of $[0,1]^2$, this time excluding corners (see Figure 1). The index set $\mathcal{I}^{BC}$ is suitably defined to account for all points in (42). Again the interpolation points on ∂V are the push-forward of (42)

$$\boldsymbol{\tau}_\nu^{BC} = \boldsymbol{F}(\hat{\boldsymbol{\tau}}_\nu^{BC}) \tag{43}$$

and then we interpolate the boundary conditions (36) and (37) at the $\boldsymbol{\tau}_\nu^{BC}$,

$$\nabla u^h(\boldsymbol{\tau}_\nu^{BC}) \cdot \boldsymbol{n} = 0, \quad \forall \nu \in \mathcal{I}^{BC} \tag{44}$$

$$\nabla(\Delta u^h)(\boldsymbol{\tau}_\nu^{BC}) \cdot \boldsymbol{n} = 0, \quad \forall \nu \in \mathcal{I}^{BC} \tag{45}$$

At the four corners of V, the normal vector $\boldsymbol{n}$ that appears in (44)-(45) is understood in an averaged sense. We note now that (41) and (44)-(45) give a total of

$$\#\mathcal{I}^C + \#\mathcal{I}^{BC} + \#\mathcal{I}^{BC} = (n^{(1)} - 4)(n^{(2)} - 4) + 4n^{(1)} + 4n^{(2)} - 8 = n^{(1)}n^{(2)} + 8$$

linear equations. Comparing to (38), it is understood that we need to reduce the number of equations. We propose the following strategy: at each corner, we average the three equations (45) that are associated to the corner point and the two adjacent points (see Figure 1). This idea seems adequate to deal with all kind of possible boundary conditions, and even though at this stage a proof of convergence is not available, our numerical examples demonstrate the viability of the approach.

To summarize, our fully discrete algorithm is as follows: Given u_n^h, find $u_{n+1}^h \in \mathcal{V}^h$ such that

$$\begin{aligned}
&u_{n+1}^h(\boldsymbol{\tau}_\nu^C) - 2\beta\delta_n\Delta u_{n+1}^h(\boldsymbol{\tau}_\nu^C) + \varepsilon^2\delta_n\Delta^2 u_{n+1}^h(\boldsymbol{\tau}_\nu^C) = \\
&u_n^h(\boldsymbol{\tau}_\nu^C) + 6\alpha\delta_n u_n^h(\boldsymbol{\tau}_\nu^C)|\nabla u_n^h(\boldsymbol{\tau}_\nu^C)|^2 + 3\delta_n(\alpha u_n^h(\boldsymbol{\tau}_\nu^C)^2 - \beta)\Delta u_n^h(\boldsymbol{\tau}_\nu^C), \quad \forall \nu \in \mathcal{I}^C \\
&\nabla(u_{n+1}^h(\boldsymbol{\tau}_\nu^{BC})) \cdot \boldsymbol{n} = 0 \quad \forall \nu \in \mathcal{I}^{BC} \\
&\nabla(\Delta u_{n+1}^h(\boldsymbol{\tau}_\nu^{BC})) \cdot \boldsymbol{n} = 0 \quad \forall \nu \in \mathcal{I}^{BC} \text{ with averaging at corners}
\end{aligned} \tag{46}$$

An example of selection of collocation and interpolation points is shown in Figure 1.

4. Numerical examples

Here we present a set of numerical examples that show the accuracy, efficiency, robustness, and geometrical flexibility of our approach. For all the numerical examples we will take $\alpha = \beta = 1$ in Eq. (2), which leads to the stable homogeneous solutions $u = \pm 1$. We will use $p = 5$ in all the numerical examples.

4.1. Accuracy test

Exact solutions to the Cahn-Hilliard equation are not available in several spatial dimensions. For this reason, we will take an adequate initial condition and solve the initial-boundary value problem (7)–(11) in two dimensions using a sufficiently small time step. We will compute the solution using different-size spatial discretizations and observe how the solution converges as we refine the spatial discretization. Following [73],

9

we will take an initial condition for which we can anticipate the behavior of the solution at early times. For this purpose, we linearize the Cahn-Hilliard equation with respect to a given concentration $\overline{u}$ within the miscibility gap, and derive the partial differential equation

$$\frac{\partial u}{\partial t} = f'(\overline{u})\Delta u - \varepsilon^2 \Delta^2 u \tag{47}$$

which approximately describes the early-time dynamics of the Cahn-Hilliard equation [6]. Now, we perform a linear stability analysis of equation (47) using small perturbations of the concentration $\overline{u}$. In particular, we take

$$u_0 = \overline{u} + \eta \cos(2\pi x/\lambda)e^{\omega t}; \quad \eta << \overline{u} \tag{48}$$

Substituting (48) in (47), we obtain an expression for the growth factor ω, namely,

$$\omega = -\left(\frac{2\pi}{\lambda}\right)^2 \left[f'(\overline{u}) + \varepsilon^2 \left(\frac{2\pi}{\lambda}\right)^2 \right] \tag{49}$$

The growth of perturbations requires $\omega > 0$, which for the remaining parameters being fixed, is achieved for

$$\lambda > \lambda_{\min} = \frac{2\pi\varepsilon}{\sqrt{-f'(\overline{u})}} \tag{50}$$

Note that equation (50) is well defined because $\overline{u}$ is in the miscibility gap, and, thus $f'(\overline{u}) < 0$. The fastest-growing mode can be obtained by maximizing ω with respect to λ. This mode is termed critical mode and is given by a wavelength λ_{cr} such that

$$\lambda_{\mathrm{cr}} = \sqrt{2}\lambda_{\min} \tag{51}$$

Substituting (51) in equation (49), we get the largest growth factor

$$\omega_{\mathrm{cr}} = \frac{f'(\overline{u})}{4\varepsilon^2} \tag{52}$$

For the above stated reasons, we will take as initial condition for our initial-boundary value problem the function

$$u_0(x,y) = \overline{u} + \eta \cos(2\pi x)\cos(2\pi y) \tag{53}$$

where $\overline{u} = 0$ and $\eta = 0.1$. Now, we will select the parameters of the Cahn-Hilliard equation so as to make the perturbations in (53) the most unstable mode. Using equations (50) and (51), we conclude that this amounts to take the computational domain $\Omega = [0,1]^2$ and $\varepsilon = 1/(4\sqrt{2}\pi)$. Taking this initial condition we expect the perturbation to grow, without creating new wavelengths, at least until the equilibrium concentrations ($u = \pm 1$) are reached. The linear analysis predicts that this will happen at a time t_s such that the amplification factor $e^{\omega_{\mathrm{cr}}t_s}$ takes the value 10. This yields a linear time scale of the order $t_s \approx 3 \cdot 10^{-2}$. After that time, the solution might bifurcate into a coarser arrangement. We have actually verified numerically that the solution achieves the equilibrium concentrations approximately at time $t \approx 5 \cdot 10^{-2}$. After that, the solution remains practically time independent until time $t_b \approx 0.2$ when it bifurcates and undergoes the typical coarsening process.

Following [73] the numerical solutions coming from different refinements will be compared at $t = 0.08$. We will use discretizations arising from uniform meshes composed of 16^2, 32^2, 64^2, and 128^2 control points. The

time step is $\delta = 10^{-4}$. To use exactly the same initial condition for all the refinements we proceed as follows: we project the function (53) onto the coarsest discretization, and then use standard knot insertion algorithms to produce identical functions on finer discretizations. This can be achieved because knot insertion generates nested discretizations in which richer spaces are supersets of coarser discretizations.

5   Figure 2(a) shows the initial condition, while Figure 2(b) presents the numerical solution on the 128^2 discretization (note that the color scale is different). The numerical solutions on the coarser meshes are almost indistinguishable from that on the 128^2 mesh. To make the differences apparent, we take horizontal cutlines of the solution at $y = 0.5$ and plot them in Figure 3. The plot shows that the solutions on different discretizations are superposed at the natural scale of the plot. Only when we zoom in (see the inset) are

10 we able to observe differences. In the inset, it is observed that the numerical approximation converges to a function, which we assume to be the exact solution. As we refine the mesh, the approximations get closer to the solution on the 128^2 discretization.

4.2. Phase separation on a square domain

A homogeneous mixture of two fluids is unstable under thermal fluctuations within the so-called miscibility

15 gap. This phenomenon is reproduced by the Cahn-Hilliard equation. A standard linear stability analysis of the Cahn-Hilliard equation reveals that homogeneous states that fall into the so-called spinodal region are unstable solutions that bifurcate into lower-free-energy states in which both phases are fully separated.

This section presents several numerical examples showing the two main separation mechanisms, namely, spinodal decomposition and nucleation[1]. The relevant mechanism in the Cahn-Hilliard equation will be

20 defined by the initial condition. We take $u_0(\boldsymbol{x}) = \overline{u} + r$, where $\overline{u}$ is a constant and r is random number uniformly distributed on $[-0.005, 0.005]$. For $\overline{u} = 0$, spinodal decomposition will be the governing separation mechanism, while for $\overline{u} \neq 0$ but within the miscibility gap, nucleation will take place. For these simulations we employ a uniform mesh composed of 512^2 control points and a constant time step $\delta = 10^{-5}$.

In the first calculation we take $\overline{u} = 0$, and let the solution evolve. The time history of the phase variable

25 u may be observed in Figure 4. The different snapshots show the typical spinodal decomposition spatial structure. The mixture separates forming a complicated striped pattern that coarsens over time. As shown in [43], if we let the simulation evolve, the stationary solution would be a fully separated flow with two rectangular patches.

In Figure 5, we show the solution for $\overline{u} = 0.4$. The rest of the parameters remain the same as in the last

30 calculation. We observe in Figure 5 that now the separation mechanism is nucleation. Isolated nuclei come up from the mixture. Again, the spatial microstructure of the mixture coarsens over time. We observe that large bubbles grow at the expense of small bubbles in consistency with the phenomenon of Ostwald ripening.

Finally, we present another example that mixes both separation mechanisms. In this case, we do not take $\overline{u}$ as a constant, but we vary it linearly with the horizontal spatial coordinate from -1 to 1. This setting gives

---

[1]In condensed matter physics literature, the word nucleation refers to the traversing of a free-energy barrier to form a new phase.

rise to three different morphologies as shown in Figure 6. On the left-hand side of the domain, the red phase nucleates into the blue one. The exact opposite occurs on the right-hand side. In the middle, where $\overline{u} \approx 0$, we observe again the striped pattern typical from spinodal decomposition. We also notice two vertical fronts that move symmetrically to the vertical boundaries of the domain ($x = 0$ and $x = 1$). The reason for this is that close to those boundaries, the initial condition approaches the pure phases which are stable solutions of the Cahn-Hilliard equation. Thus, phase separation on those parts of the domain is very slow or even inexistent. Figure 7 shows the time evolution of the free-energy functional $\mathcal{G}$ for the spinodal decomposition (Figure 7(a)), the nucleation example (Figure 7(b)), and the mixed decomposition (Figure 7(c)). We observe that the free energy is decreasing at all times, which is consistent with the behavior of the exact solution.

4.3. Rupture of thin liquid columns during phase separation

In this example we use the Cahn-Hilliard equation to simulate the rupture of thin liquid columns during phase separation. The computational mesh is composed of 512^2 control points and the time step is $\delta = 10^{-5}$. We embed into a fully separated phase ($u = -1$) three columns of a mixture with a concentration in the miscibility gap, as shown in Figure 8(a). The thickness of the liquid columns is 0.05 with sinusoidal perturbations. The three columns are composed of mixtures with different concentrations, leading to different rupture topologies as shown in the snapshots of Figure 8. The liquid column on the left is defined by the concentration -0.26, the one in the middle by -0.32, and that on the right by -0.38. It is shown in the simulation that the closer to the spinodal decomposition regime the column concentration is, the more elongated the drops are (left column). As we approach the nucleation regime (right column), the drops become isolated circular spots as one would expect. Finally, we note that Figure 9 shows that the free energy of the discrete solution is time decreasing.

4.4. Phase separation on mapped domains

Here we show the geometrical flexibility of our method by solving the Cahn-Hilliard equation on mapped geometries. We will illustrate the methodology using a quarter of an annulus and a circle, but more general geometries can be utilized. The NURBS geometrical mapping that transforms the parametric space (a square) into a quarter of an annulus can be found, for example, in [28]. The mapping that transforms the parametric domain into a circle can be found in [71]. We wish to emphasize that, due to the use of NURBS, the geometrical representation of the computational domain is exact. To apply our collocation method on the mapped geometry, the partial derivatives of the discrete solution in the physical space are obtained simply using the chain rule.

4.4.1. Phase separation on a quarter of an annulus

In this example, we take an annulus with internal radius $r_i = 1$ and external radius $r_e = 4$. The mesh is composed of 256^2 control points and the time step is $\delta = 10^{-4}$. The interface length scale is given by $\varepsilon^2 = 10^{-3}$. We solve a nucleation example taking as initial condition a random perturbation of the homogeneous state $\overline{u} = 0.4$. Figure 10 shows snapshots of the time history of the numerical solution. We

observe again the typical spatial pattern of nucleation in which bigger bubbles grow at the expense of smaller bubbles, leading to microstructure coarsening over time.

4.4.2. Phase separation on a circle

In this final example, we consider a circle of radius $r = 4$. We remark that the adopted mapping [71] gives rise to four singular points lying on the boundary of the domain. Such points naturally lack the minimum regularity required for the imposition of Neumann boundary conditions. This kind of problems can be simply solved for instance by resorting to multi-patch geometries comprised of regular patches. Multi-patch conditions for isogeometric collocation have been discussed and successfully applied in the framework of elasticity [9], but it is out of the scope of the present paper to extend them to the case under investigation.

However, we decided to consider this problem to have the opportunity to illustrate the flexibility of our method with respect to boundary conditions, showing how to impose in a simple and straighforward way Dirichlet conditions (which amounts to taking $\partial V_N = \emptyset$ in (9))[2]. As initial condition we will take a random perturbation of the homogeneous state $\overline{u} = 0$. Then, to make the boundary conditions compatible with the initial conditions, we take $u_D = 0$ in (8). As a consequence, we have to impose (8) and (10) on the boundary. These boundary conditions can be imposed strongly in the spline space $\mathcal{V}^h$ by removing the basis functions that are not zero or have not zero derivatives at the boundary (as shown in [7] in the context of the solution of different fourth order PDEs by means of standard Galerkin-based isogeometric analysis). The computational mesh is composed of 256^2 control points, and the time step is $\delta = 10^{-4}$. The interface length scale is given by $\varepsilon^2 = 10^{-3}$. The time history of the phase variable is shown in Figure 11 which shows the coarsening dynamics of the mixture subjected to Dirichlet boundary conditions. Figure 12 shows the time evolution of the free energy for the numerical examples on mapped geometries. We note that the free energy is time decreasing in both cases, although for the example on a circle that does not have to be necessarily the case, because that property no longer holds for the exact solution when Dirichlet boundary conditions are imposed.

5. Conclusions

We have presented isogeometric collocation methods for phase-field models. We have illustrated the ideas behind our method by discretizing the Cahn-Hilliard equation, which is one of the most widely utilized phase-field models. We have presented several numerical examples involving the phase separation of two-phase immiscible systems. The numerical examples show the accuracy, efficiency, and geometrical flexibility of our method, which we believe successfully combines geometrical flexibility with simplicity and efficiency.

---

[2]We remark that the strategy described in Section 3.2.5 can be successfully used also to impose Dirichlet boundary conditions. However, since the strategy proposed here is a simple and straigthforward alternative which is also able to deal with Dirichlet conditions on a boundary with singular points, we believe that it is worthwhile to show an example where it is used.

6. Acknowledgements

References

[1] I. Akkerman, Y. Bazilevs, V. M. Calo, T. J. R. Hughes, S. Hulshoff, The role of continuity in residual-based variational multiscale modeling of turbulence, *Computational Mechanics* **41** 371–378, 2007.

[2] D. Anders, K. Weinberg, Numerical simulation of diffusion induced phase separation and coarsening in binary alloys, *Computational Materials Science* **50** 1359–1364, 2011.

[3] D. Anders, A. Hoffmann, H.-P. Scheffler, K. Weinberg, Application of operator-scaling anisotropic random fields to binary mixtures, *Philosophical Magazine* **91** 3766–3792, 2011.

[4] D. Anders, C. Hesch, K. Weinberg, Computational modeling of phase separation and coarsening in solder alloys, *International Journal of Solids and Structures*, **49** 1557–1572 ,2012.

[5] D.M. Anderson, G.B. McFadden, A.A. Wheeler, Diffuse-interface methods in fluid mechanics, *Annu. Rev. Fluid Mech.* **30** 139–165, 1998.

[6] S. Asai, S. Majumdar, A. Gupta, K. Kargupta, S. Ganguly, Dynamics and patter formation in thermally induced phase separation of polymer-solvent system, *Computational Materials Science*, **47** 193–205, 2009.

[7] F. Auricchio, L. Beirao da Veiga, A. Buffa, C. Lovadina, A. Reali, G. Sangalli, A Fully Locking-free Isogeometric Approach for Plane Linear Elasticity Problems: a Stream Function Formulation, *Computer Methods in Applied Mechanics and Engineering*, **197** 160–172, 2007.

[8] F. Auricchio, L. Beirao da Veiga, T.J.R. Hughes, A. Reali, G. Sangalli, Isogeometric Collocation Methods, *Mathematical Models and Methods in Applied Sciences*, **20** 2075–2107, 2010.

[9] F. Auricchio, L. Beirao da Veiga, T.J.R. Hughes, A. Reali, G. Sangalli, Isogeometric collocation for elastostatics and explicit dynamics, *Computer Methods in Applied Mechanics and Engineering*, **249-252** 1043–1055, 2012.

[10] F. Auricchio, L. Beirão da Veiga, C. Lovadina, A. Reali, The importance of the exact satisfaction of the incompressibility constraint in nonlinear elasticity: mixed FEMs versus NURBS-based approximations. *Computer Methods in Applied Mechanics and Engineering*, **199** 314–323, 2010.

[11] F. Auricchio, L. Beirao da Veiga, J. Kiendl, C. Lovadina, A. Reali, Locking-free isogeometric colloca-tion methods for spatial Timoshenko rods, submitted to *Computer Methods in Applied Mechanics and Engineering*, 2012.

[12] V.E. Badalasi, H.D. Ceniceros, S. Banerjee, Computation of multiphase systems with phase field models, *Journal of Computational Physics*, **190** 371–397, 2003.

[13] Y. Bazilevs, V.M. Calo, J.A. Cottrell, J.A. Evans, T.J.R. Hughes, S. Lipton, M.A. Scott, T.W. Sederberg, Isogeometric Analysis using T-splines, *Computer Methods in Applied Mechanics and Engineering*, **199** 229–263, 2010.

[14] Y. Bazilevs, V.M. Calo, J.A. Cottrell, T.J.R. Hughes, A. Reali, G. Scovazzi, Variational multiscale residual-based turbulence modeling for large eddy simulation of incompressible flows, *Computer Methods in Applied Mechanics and Engineering* **197** 173–201, 2007.

[15] Y. Bazilevs, T.J.R. Hughes, NURBS-based isogeometric analysis for the computation of flows about rotating components, *Computational Mechanics* **43** 143–150, 2008.

[16] J. Becker, G. Grün, R. Seemann, H. Mantz, K. Jacobs, K.R. Mecke, R. Blossey, Complex dewetting scenarios captured by thin-film models, *Nature Materials* **2** 59–63, 2003.

[17] L. Beirao da Veiga, A. Buffa, J. Rivas, G. Sangalli, Some estimates for *h-p-k*-refinement in Isogeometric Analysis, *Numerische Mathematik* **118**, 271–305, 2011.

[18] L. Beirao da Veiga, C. Lovadina, A. Reali, Avoiding shear locking for the Timoshenko beam problem via isogeometric collocation methods, *Computer Methods in Applied Mechanics and Engineering* **249-252** 2–14, 2012.

[19] L. Beirao da Veiga, G. Sangalli, Anisotropic NURBS approximation in Isogeometric Analysis, *Computer Methods in Applied Mechanics and Engineering* **209-212**, 1–11, 2012.

[20] M.J. Borden, C.V. Verhoosel, M.A. Scott, T.J.R. Hughes, C.M. Landis, A phase-field description of dynamic brittle fracture, *Computer Methods in Applied Mechanics and Engineering* **217** 77–95, 2012.

[21] A. Buffa, C. de Falco, G. Sangalli, IsoGeometric Analysis: Stable elements for the 2D Stokes equation, *International Journal for Numerical Methods in Fluids* **65**, 1407–1422, 2011.

[22] A. Buffa, G. Sangalli, R. Vázquez, Isogeometric analysis in electromagnetics: B-splines approximation, *Computer Methods in Applied Mechanics and Engineering* **199** 1143–1152, 2010.

[23] J.W. Cahn, J.E. Hilliard, Free energy of a non-uniform system. I. Interfacial free energy, *The Journal of Chemical Physics* **28** 258–267, 1958.

[24] J.W. Cahn, J.E. Hilliard, Free energy of a non-uniform system. III. Nucleation in a two-component incompressible fluid, *The Journal of Chemical Physics* **31** 688–699, 1959.

[25] H.D. Ceniceros, R.L. Nós, A.M. Roma, Three-dimensional, fully adaptive simulations of phase-field fluid models, *Journal of Computational Physics*, **229** 6135–6155, 2010.

[26] L.Q. Chen, Phase-field models for microstructural evolution, *Ann. Rev. Mater. Res.* **32** 113–140, 2002.

[27] R. Choksi, M.A. Peletier, and J.F. Williams, On the phase diagram for microphase separation of diblock copolymers: an approach via a nonlocal Cahn-Hilliard functional, *SIAM Journal of Applied Mathematics*, **69** 1712–1738, 2009.

[28] J.A. Cottrell, T.J.R. Hughes, Y. Bazilevs, Isogeometric Analysis: Toward integration of CAD and FEA, Wiley, 2009.

[29] J.A. Cottrell, T.J.R. Hughes, A. Reali, Studies of refinement and continuity in isogeometric structural analysis, *Computer Methods in Applied Mechanics and Engineering*, **196** 4160–4183, 2007.

[30] J.A. Cottrell, A. Reali, Y. Bazilevs, T.J.R. Hughes, Isogeometric Analysis of Structural Vibrations, *Computer Methods in Applied Mechanics and Engineering*, **195** 5257–5296, 2006.

[31] L. Cueto-Felgueroso, R. Juanes, Nonlocal interface dynamics and pattern formation in gravity-driven unsaturated flow through porous media, *Physical Review Letters* **101** 244504, 2008.

[32] L. Cueto-Felgueroso, R. Juanes, A phase-field model of unsaturated flow, *Water Resources Research*, **45** W10409, 2009.

[33] L. Cueto-Felgueroso, R. Juanes, Adaptive rational spectral methods for the linear stability analysis of nonlinear fourth-order problems, *Journal of Computational Physics*, **228** 6536–6552, 2009.

[34] C. de Falco, A. Reali, R. Vázquez. GeoPDEs: a research tool for IsoGeometric Analysis of PDEs, *Advances in Engineering Software*, **42** 1020–1034, 2011.

[35] Q. Du, R.A. Nicolaides, Numerical analysis of a continuum model of phase transition, *SIAM Journal of Numerical Analysis* **28** 1310–1322, 1991.

[36] K.R. Elder, M. Grant, Modeling elastic and plastic deformations in nonequilibrium processing using phase field crystals, *Physical Review E* **70** 051605, 2004.

[37] K.R. Elder, M. Katakowski, M. Haataja, M. Grant, Modeling elasticity in crystal growth, *Physical Review Letters* **88** 245701, 2002.

[38] T. Elguedj, Y. Bazilevs, V.M. Calo, T.J.R. Hughes, $\bar{B}$ and $\bar{F}$ projection methods for nearly incompressible linear and non-linear elasticity and plasticity using higher-order NURBS elements, *Computer Methods in Applied Mechanics and Engineering* **197** 2732–2762, 2008.

[39] H. Emmerich, *The diffuse interface approach in materials science*, Springer, 2003.

[40] D.J. Eyre, An unconditionally stable one-step scheme for gradient systems, unpublished, www.math.utah.edu/~eyre/research/methods/stable.ps

[41] J.A. Evans, Y. Bazilevs, I. Babuška, T.J.R. Hughes, n-widths, sup infs, and optimality ratios for the k-version of the isogeometric finite element method, *Computer Methods in Applied Mechanics and Engineering*, **198** 1726–1741, 2009.

[42] D. Furihata, A stable and conservative finite difference scheme for the Cahn-Hilliard equation, *Numer. Math.* **87** 675–699, 2001.

[43] H. Gomez, V.M. Calo, Y. Bazilevs, T.J.R. Hughes, Isogeometric analysis of the Cahn-Hilliard phase-field model, *Computer Methods in Applied Mechanics and Engineering* **197** 4333–4352, 2008.

[44] H. Gomez, T.J.R. Hughes, X. Nogueira, V.M. Calo, Isogeometric analysis of the isothermal Navier-Stokes-Korteweg equations, *Computer Methods in Applied Mechanics and Engineering* **199** 1828–1840, 2010.

[45] H. Gomez, T.J.R. Hughes, Provably unconditionally stable, second-order time-accurate, mixed variational methods for phase-field models, *Journal of Computational Physics*, **230**, 5310–5327, 2011.

[46] H. Gomez, X. Nogueira, An unconditionally energy-stable method for the phase-field crystal equation, *Computer Methods in Applied Mechanics and Engineering* **249–252**, 52–61, 2012.

[47] H. Gomez, X. Nogueira, A new space-time discretization for the Swift-Hohenberg equation that strictly respects the Lyapunov functional, *Communications in Nonlinear Science and Numerical Simulation* **17**(12), 4930–4946, 2012.

[48] H. Gomez, J. París, Numerical simulation of asymptotic states of the damped Kuramoto-Sivashinsky equation, *Physical Review E*, **83**, 046703, 2011.

[49] F. Guillén-González, G. Tierra, On linear schemes for a CahnHilliard diffuse interface model, *Journal of Computational Physics*, **234**, 140–171, 2013.

[50] Z. Guo, J. Mi, P.S. Grant, An implicit parallel multigrid computing scheme to solve coupled thermal-solute phase-field equations for dendrite evolution, *Journal of Computational Physics*, **231** 1781–1796, 2012.

[51] M.E. Gurtin, Generalized Ginzburg-Landau and Cahn-Hilliard equations based on a microforce balance, *Physica D*, **92** 178–192, 1996.

[52] L. He, Y. Liu, A class of stable spectral methods for the Cahn-Hilliard equation, *Journal of Computational Physics*, **228** 5101–5110, 2009.

[53] Z. Hu, S.M. Wise, C. Wang, J.S. Lowengrub, Stable and efficient finite-difference nonlinear multigrid schemes for the phase field crystal equation, *Journal of Computational Physics*, **228** 5323–5339, 2009.

[54] T.J.R. Hughes, *The Finite Element Method: Linear Static and Dynamic Finite Element Analysis*, Dover Publications, Mineola, NY, 2000.

17

[55] T.J.R. Hughes, J.A. Cottrell, Y. Bazilevs, Isogeometric analysis: CAD, finite elements, NURBS, exact geometry and mesh refinement, *Computer Methods in Applied Mechanics and Engineering*, **194** 4135–4195, 2005.

[56] T.J.R Hughes, A. Reali, G. Sangalli, Duality and unified analysis of discrete approximations in structural dynamics and wave propagation: comparison of p-method finite elements with k-method NURBS, *Computer Methods in Applied Mechanics and Engineering*, **197** 4104–4124, 2008.

[57] J. Kim, Phase field computations for ternary fluid flows, *Computer Methods in Applied Mechanics and Engineering*, **196** 4779–4788, 2007.

[58] J. Kiendl, K.-U. Bletzinger, J. Linhard, R. Wüchner, Isogeometric Shell Analysis with Kirchhoff-Love Elements, *Computer Methods in Applied Mechanics and Engineering*, **198** 3902–3914, 2009.

[59] S. Lipton, J.A. Evans, Y. Bazilevs, T. Elguedj, T.J.R. Hughes, Robustness of isogeometric structural discretizations under severe mesh distortion, *Computer Methods in Applied Mechanics and Engineering*, **199** 357–373, 2010.

[60] J.S. Lowengrub, L. Truskinovsky, Quasi-incompressible Cahn-Hilliard Fluids and Topological Transitions, *Proceedings of the Royal Society London A*, **454** 2617–2654, 1998.

[61] D.R. Mahapatra, R.V.N. Melnik, Finite element analysis of phase transformation dynamics in shape memory alloys with a consistent Landau-Ginzburg free energy model, *Mechanics of Advanced Materials and Structures*, **13** 443–455, 2006.

[62] D.R. Mahapatra, R.V.N. Melnik, Finite element approach to modelling evolution of 3D shape memory materials, *Mathematics and Computers in Simulation*, **76** 141–148, 2007.

[63] L.M. Pismen, *Patterns and interfaces in dissipative dynamics*, Springer, 2005.

[64] A. Reali, An Isogeometric Analysis Approach for the Study of Structural Vibrations, *Journal of Earthquake Engineering*, **10**, 1–30, 2006.

[65] D. Schillinger, J.A. Evans, A. Reali, M.A. Scott, T.J.R. Hughes, Isogeometric Collocation: Cost Comparison with Galerkin Methods and Extension to Adaptive Hierarchical NURBS Discretizations, *ICES Reports*, **13-03**, 2013.

[66] J. Shen, X. Yang, An efficient moving mesh spectral method for the phase-field model of two phase flows, *Journal of Computational Physics*, **228** 2978–2992, 2009.

[67] J. Shin, D. Jeong, J. Kim, A conservative numerical method for the Cahn-Hilliard equation in complex domains, *Journal of Computational Physics*, **230** 7441–7455, 2011.

[68] R.H. Stogner, G.F. Carey, B.T. Murray, Approximation of CahnHilliard diffuse interface models using parallel adaptive mesh refinement and coarsening with C^1 elements, *International Journal for Numerical Methods in Engineering*, **76** 636–661, 2008.

[69] G. Tegze, G. Bansel, G.I. Tóth, T. Pusztai, Z. Fan, L. Gránásy, Advanced operator splitting-based semi-implicit spectral method to solve the binary phase-field crystal equations with variable coefficients, *Journal of Computational Physics*, **228** 1612–1623, 2009.

[70] S. Tremaine, On the origin of irregular structure in Saturn's rings, *Astronomical Journal* **125** 894–901, 2003.

[71] A.-V. Vuong, Ch. Heinrich, B. Simenon, ISOGAT: A 2D tutorial MATLAB code for Isogeometric Analysis, *Computer Aided Geometric Design*, **27**, 644–655, 2010.

[72] Y. Xia, Y. Xu, C.-W. Shu, Local discontinuous Galerkin methods for the Cahn-Hilliard type equations , *Journal of Computational Physics*, in press.

[73] O. Wodo, B. Ganapathysubramanian, Computationally efficient solution to the Cahn-Hilliard equation: Adaptive implicit time schemes, mesh sensitivity analysis and the 3D isoperimetric problem, *Journal of Computational Physics*, **230** 6037–6060, 2011.

19
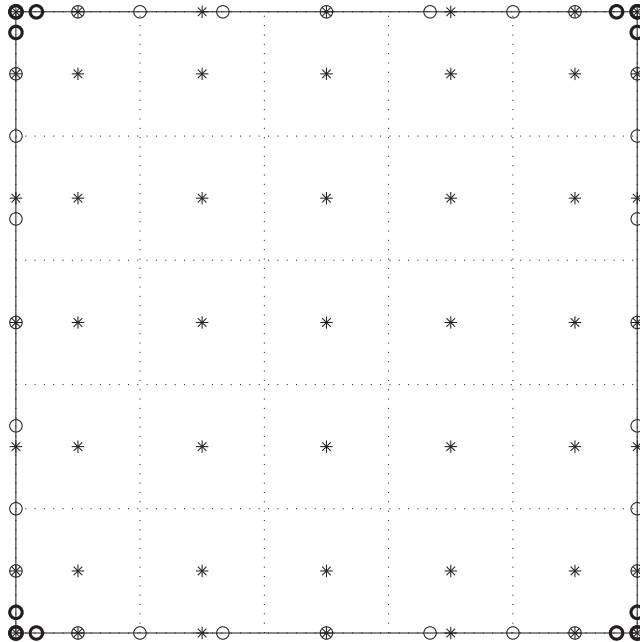
Figure 1: Example of collocation points and boundary condition interpolation points. We consider the parametric domain, we set degree $p = 5$ and the knot vector $\boldsymbol{K} = (0, 0, 0, 0, 0, 0, .2, .4, .6, .8, 1, 1, 1, 1, 1, 1)$ in each direction. The collocation points from (39) are represented by stars, the interpolation points (42) for the boundary conditions are indicated by circles. The boundary condition (45) is averaged at each corner on the thick circles.
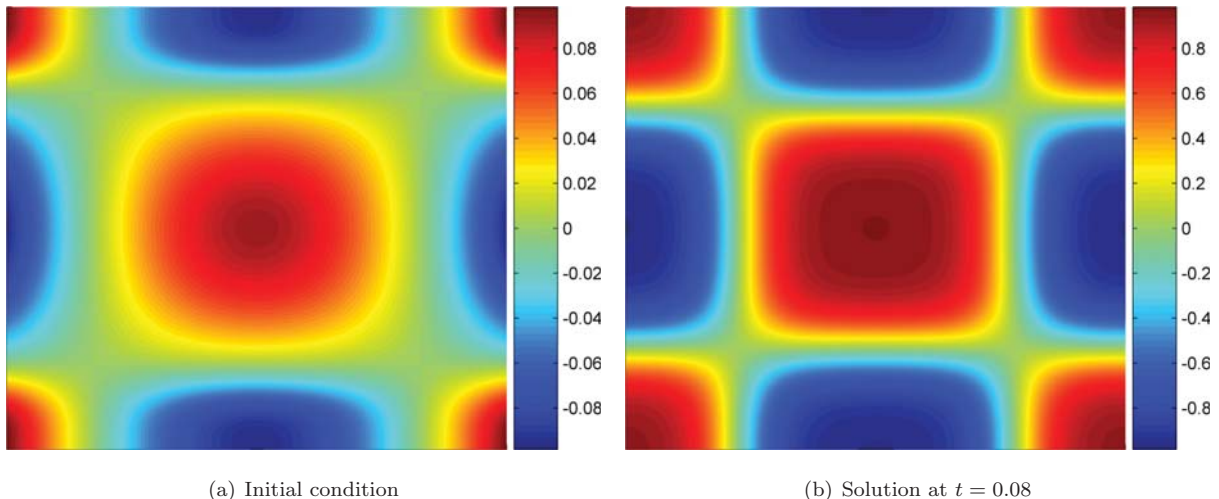

(a) Initial condition

(b) Solution at $t = 0.08$

Figure 2: Accuracy test. The initial condition, shown in panel (a), represents the most unstable mode for the Cahn-Hilliard equation in the linear regime. When we advance the solution in time, the perturbations with respect to the homogeneous state $\overline{u} = 0$ grow leading to the solution in panel (b) at time $t = 0.08$ (note that the color scale is different). We computed the solution on meshes composed of 16^2, 32^2, 64^2, and 128^2 control points, and they were almost indistinguishable at the scale of the plot (here we show the solution on the finest mesh).
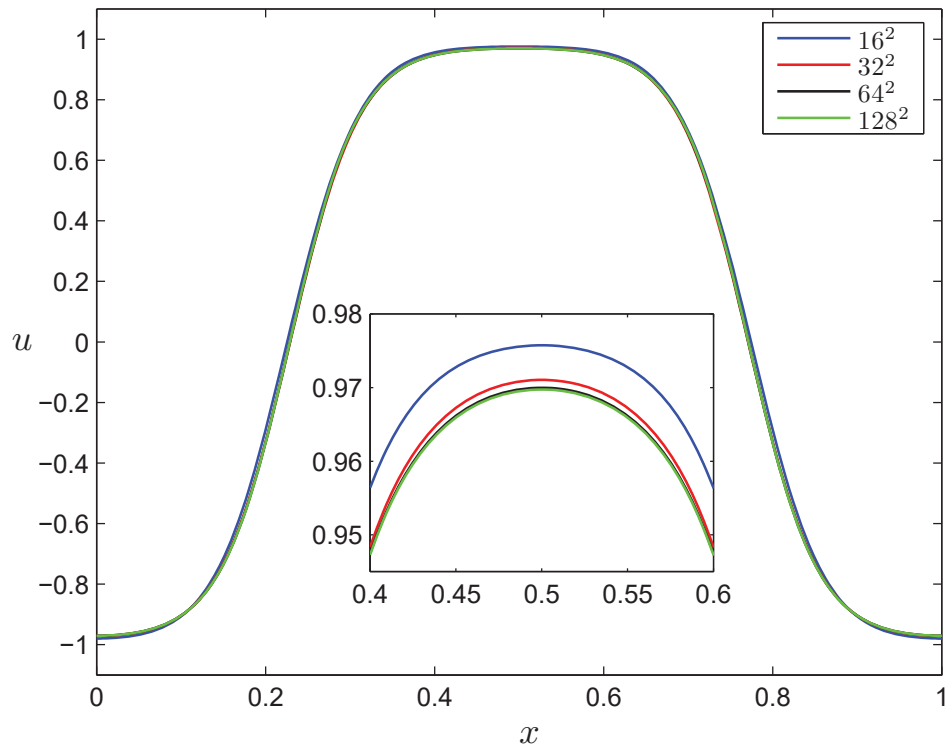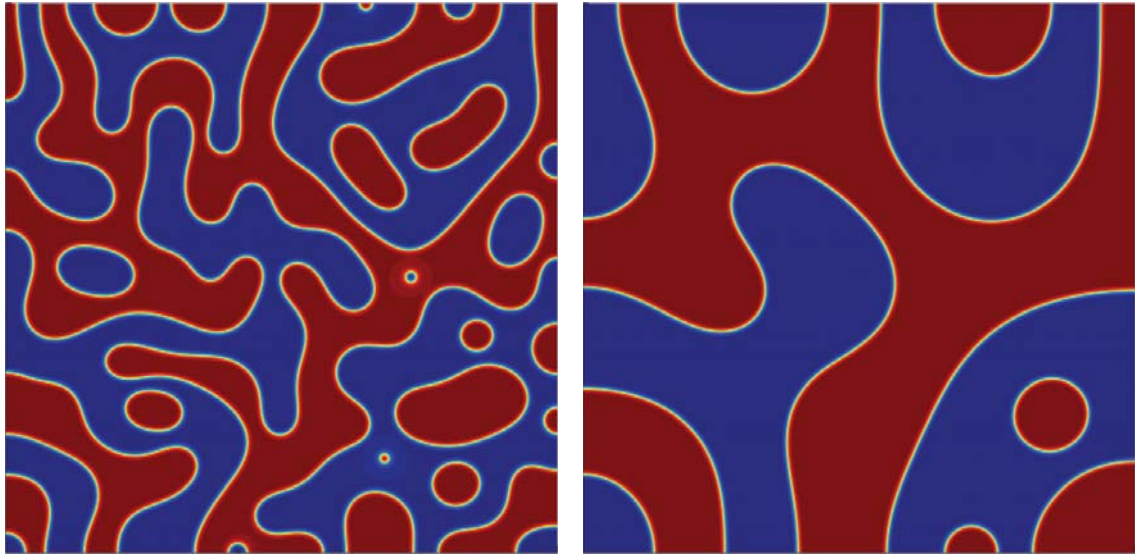
Figure 3: Accuracy test. Comparison of the numerical solutions computed on uniform meshes composed of 16^2, 32^2, 64^2, and 128^2 control points. We took horizontal cutlines (at $y = 0.5$) of the solution to the problem shown in Figure 2(b). The inset shows an amplified view of the interval $x \in [0.4, 0.6]$.
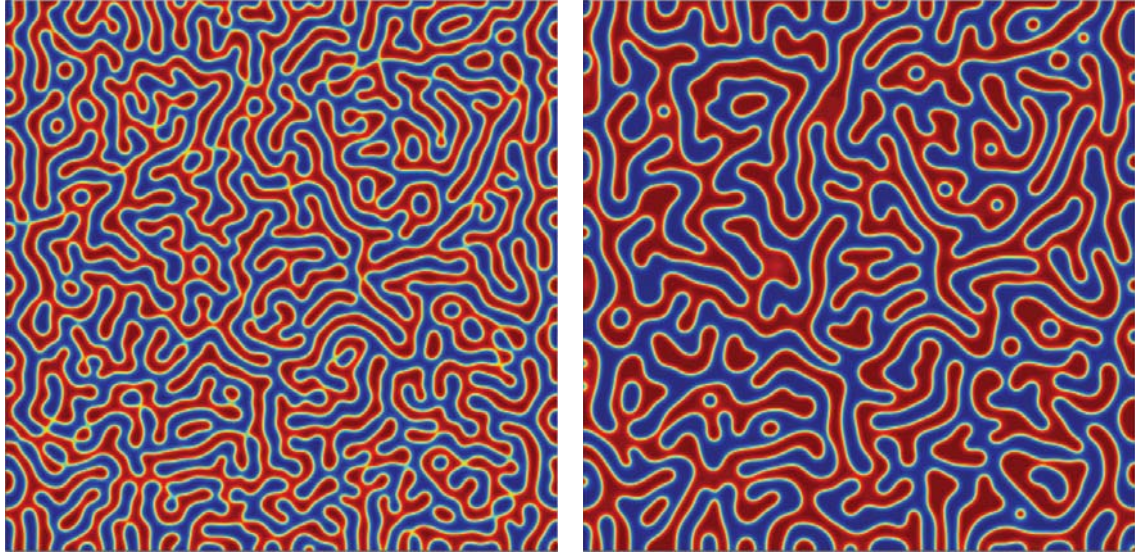
(a) $t = 2 \cdot 10^{-3}$

(b) $t = 4 \cdot 10^{-3}$

(c) $t = 5 \cdot 10^{-2}$

(d) $t = 5 \cdot 10^{-1}$

Figure 4: Phase separation on a square domain. The governing separation mechanism is spinodal decomposition. The mixture separates from a randomly perturbed homogeneous state ($\overline{u} = 0$) giving rise to a striped pattern of complicated topology that coarsens over time. The mesh is composed of 512^2 control points. The parameters are $\varepsilon^2 = \delta = 10^{-5}$.

(a) $t = 4 \cdot 10^{-3}$

(b) $t = 1 \cdot 10^{-2}$

(c) $t = 5 \cdot 10^{-2}$

(d) $t = 5 \cdot 10^{-1}$
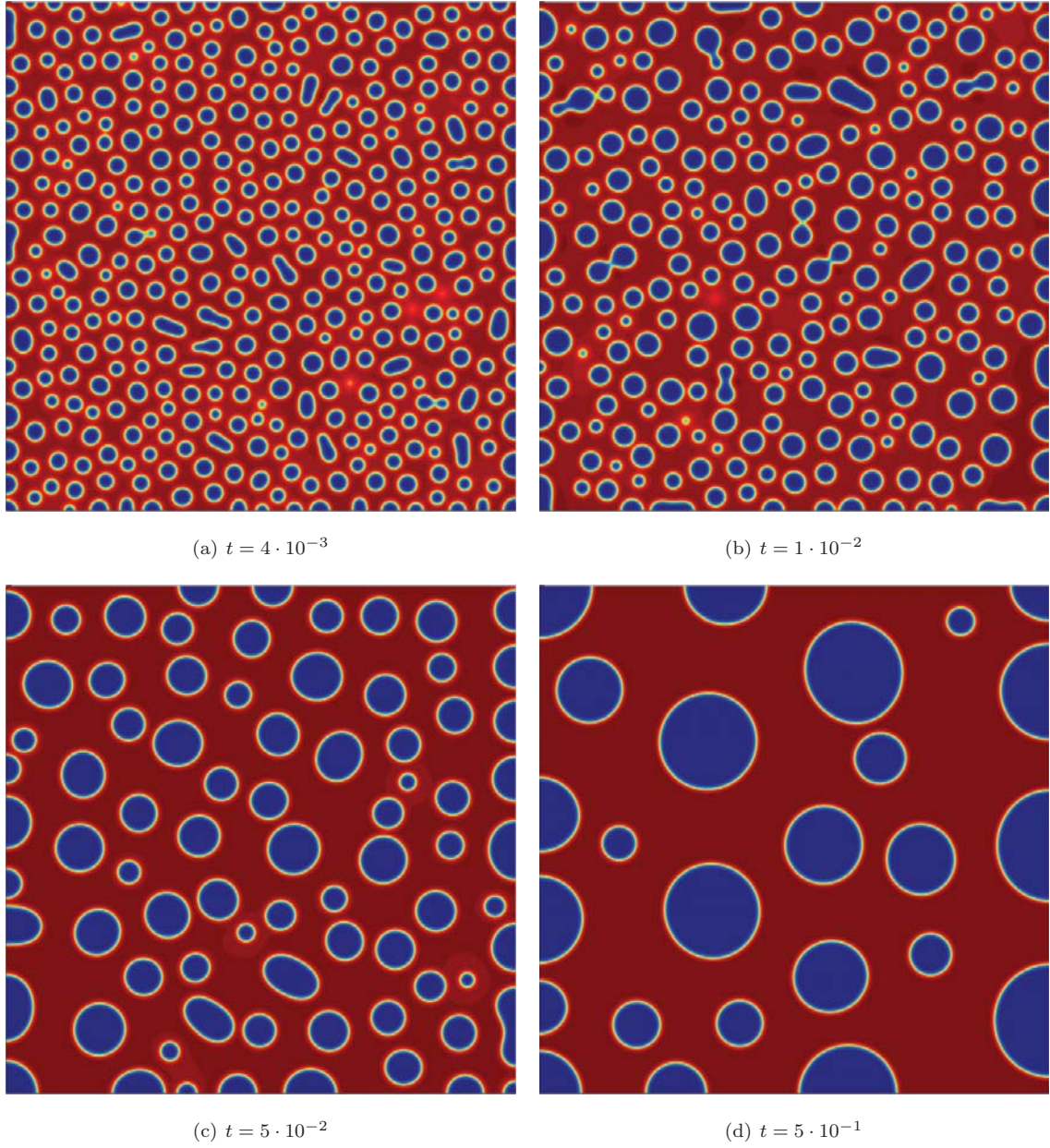
Figure 5: Phase separation on a square domain. The governing separation mechanism is nucleation. The mixture separates from a randomly perturbed homogeneous state ($\overline{u} = 0.4$) giving rise to a spatial structure composed of isolated circular patches whose size increases with time. The mesh is composed of 512^2 control points. The parameters are $\varepsilon^2 = \delta = 10^{-5}$.

(a) $t = 1 \cdot 10^{-3}$

(b) $t = 2 \cdot 10^{-3}$

(c) $t = 6 \cdot 10^{-3}$

(d) $t = 1.5 \cdot 10^{-1}$
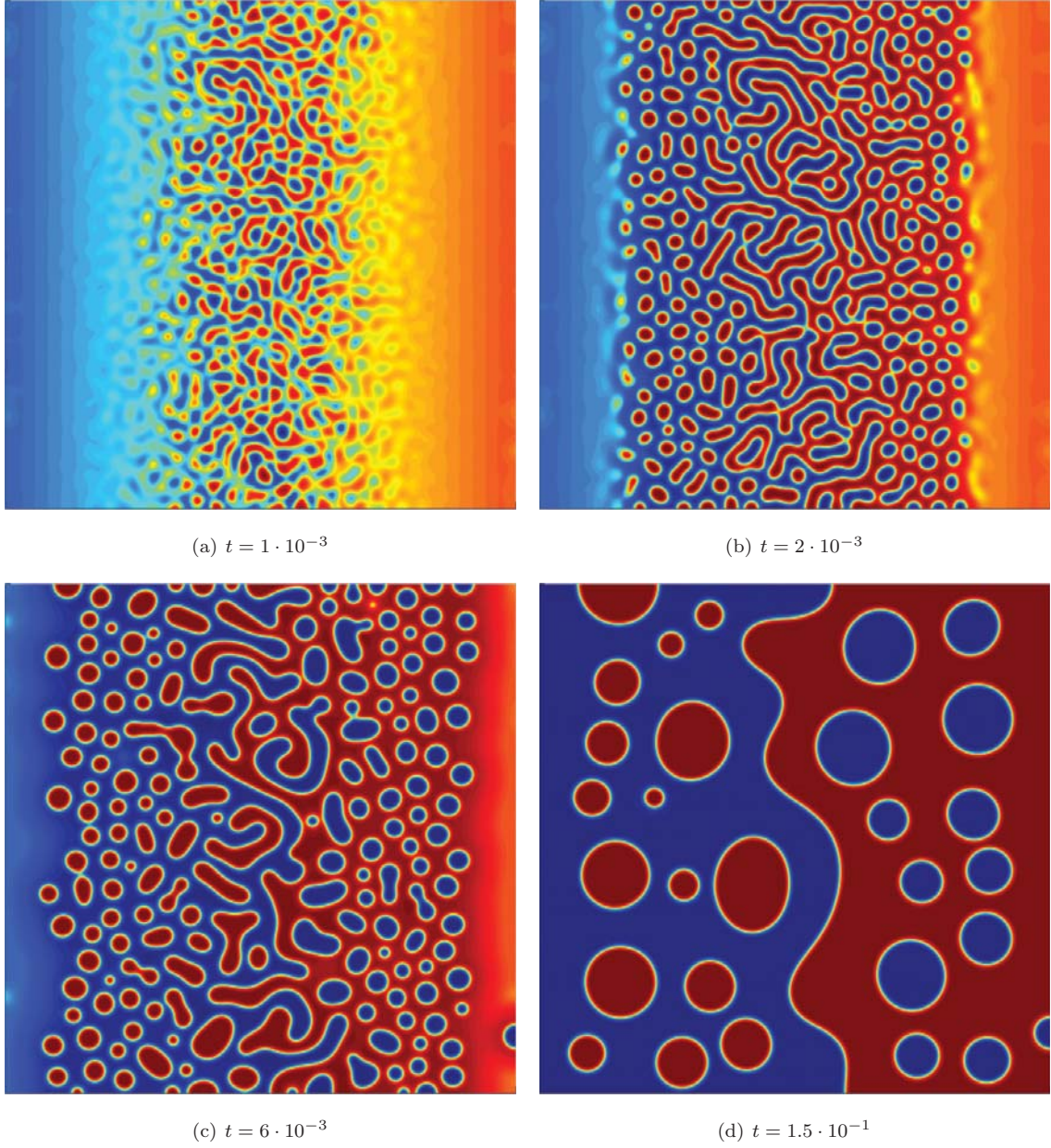
Figure 6: Phase separation on a square domain from a randomly perturbed linear state $\bar{u} = 2(x - 0.5)$. Both spinodal decomposition and nucleation take place on different parts of the computational domain. The mesh is composed of 512^2 control points. The parameters are $\varepsilon^2 = \delta = 10^{-5}$.
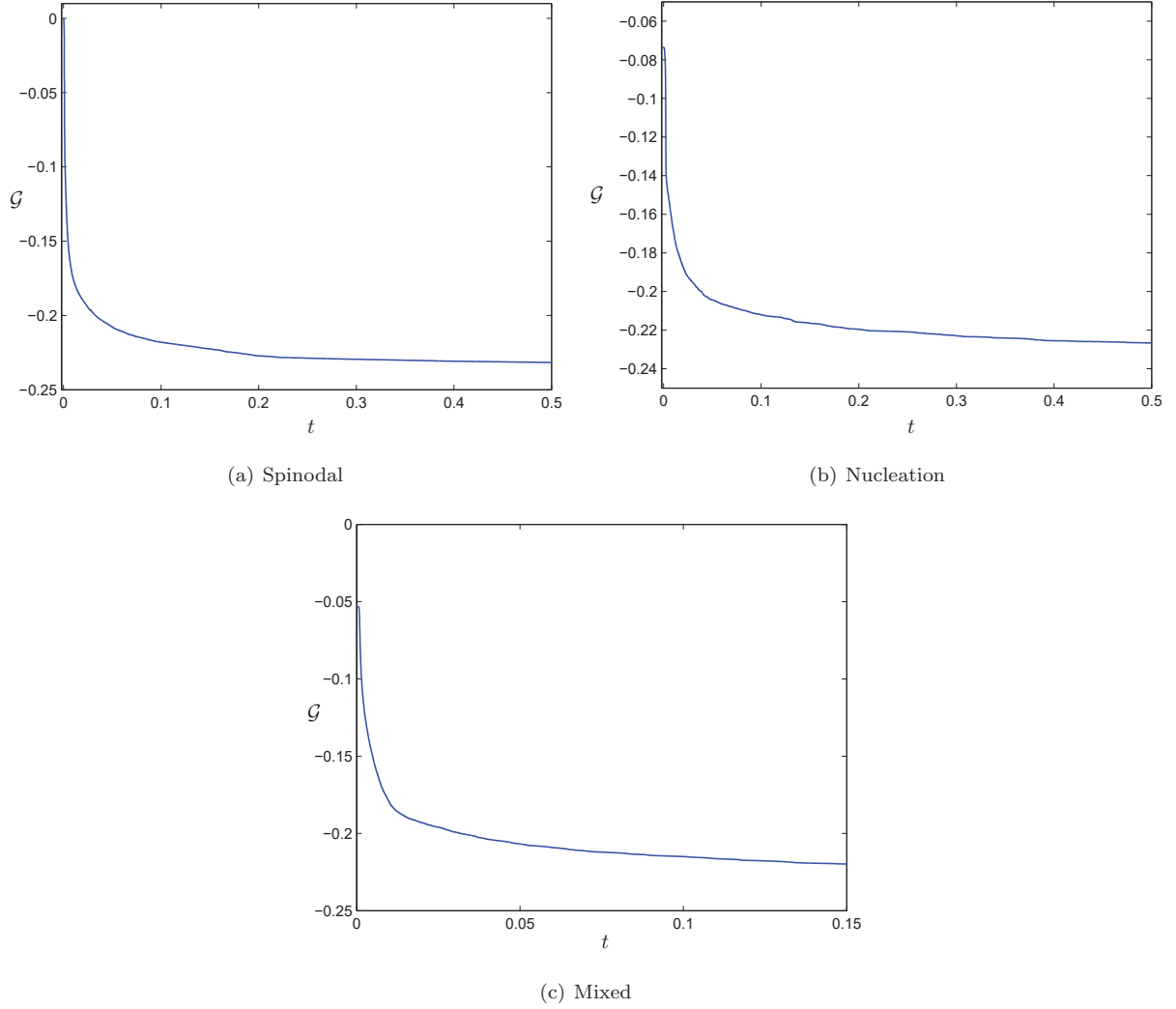
(a) Spinodal

(b) Nucleation

(c) Mixed

Figure 7: Phase separation on a square domain. Time evolution of the free energy funtional $\mathcal{G}$ of the discrete solution. We observe that $\mathcal{G}$ is monotonically decreasing, indicating that the discrete solution respects the underlying physics of the problem. Panel (a) corresponds to the spinodal decomposition. The parameters are $\varepsilon^2 = \delta = 10^{-5}$ and $\overline{u} = 0$. Panel (b) corresponds to nucleation. The parameters are $\varepsilon^2 = \delta = 10^{-5}$ and $\overline{u} = 0.4$. Panel (c) corresponds to the mixed separation mechanism in which spinodal decomposition and nucleation take place simultaneously. The parameters are $\varepsilon^2 = \delta = 10^{-5}$ and $\overline{u} = 2(x - 0.5)$.

(a) $t = 0$

(b) $t = 2 \cdot 10^{-4}$

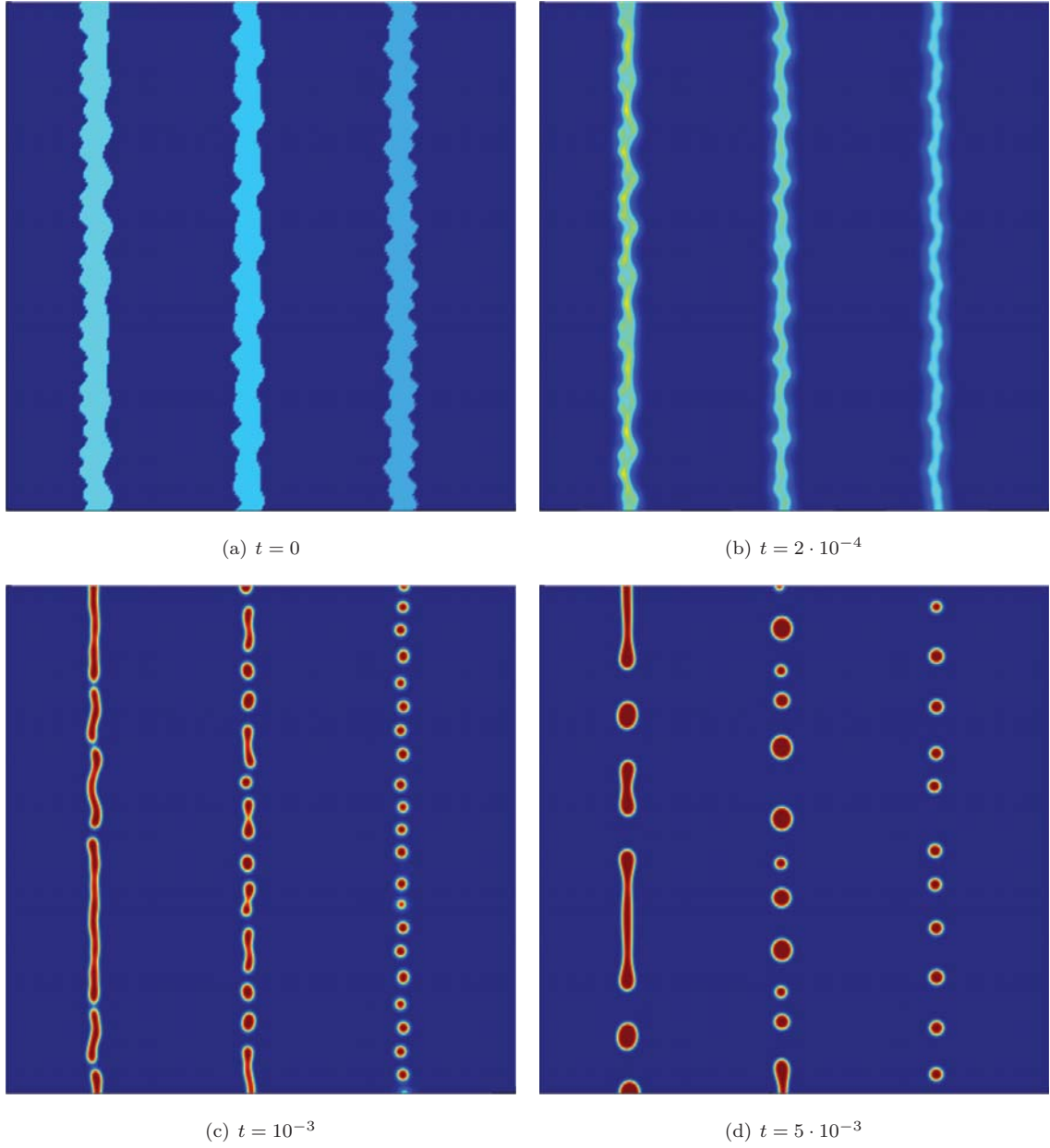(c) $t = 10^{-3}$

(d) $t = 5 \cdot 10^{-3}$

Figure 8: Rupture of thin liquid columns during phase separation. The images show how different mixture concentration in the liquid columns lead to different rupture patterns. The mesh is composed on 512^2 control points. The parameters are $\varepsilon^2 = \delta = 10^{-5}$.
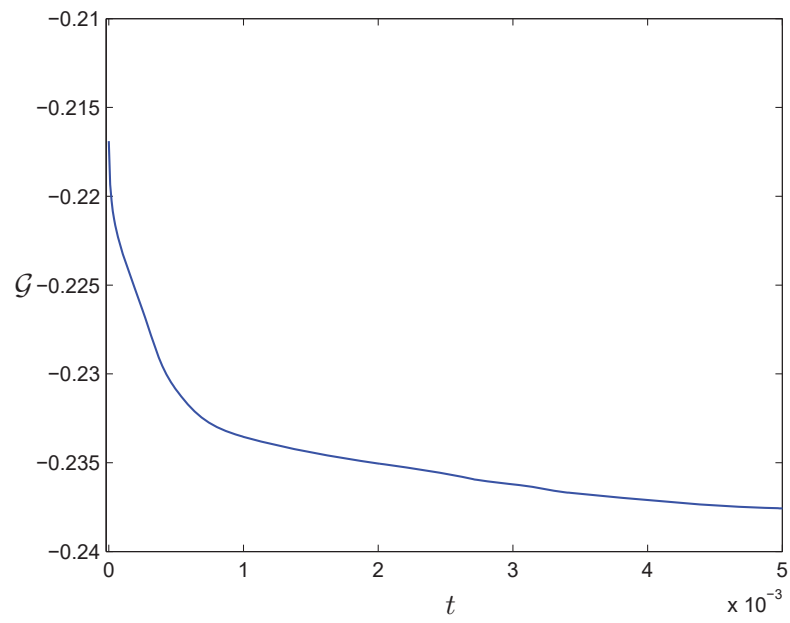
Figure 9: Phase separation on a square domain. We plot the time evolution of the free energy funtional $\mathcal{G}$, which is monotonically decreasing. This behavior is consistent with that of the exact solution. The parameters are $\varepsilon^2 = \delta = 10^{-5}$.
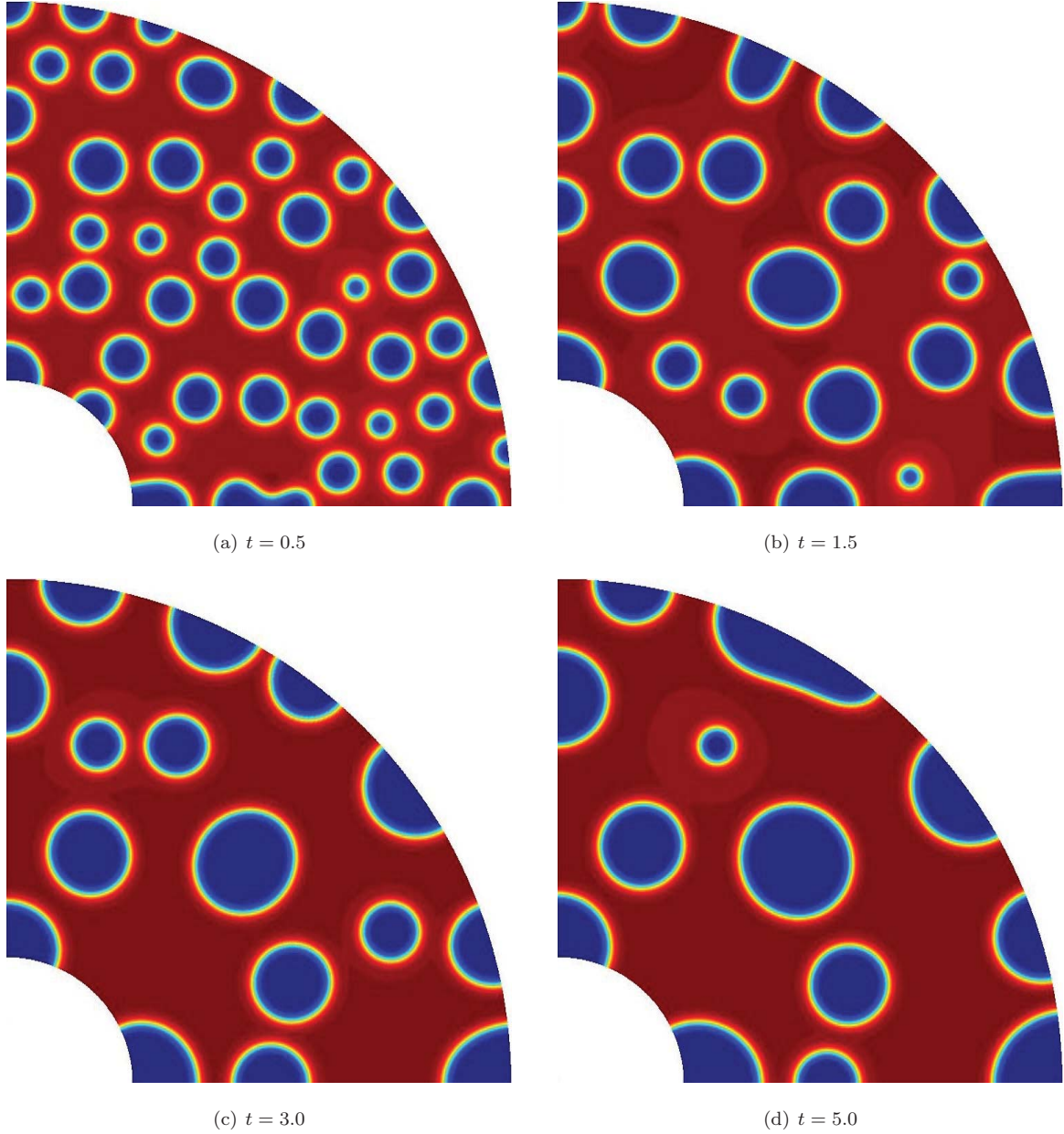
(a) $t = 0.5$

(b) $t = 1.5$

(c) $t = 3.0$

(d) $t = 5.0$

Figure 10: Nucleation on a quarter of an annulus. The exterior radius is $r_e = 4$, while the interior is $r_i = 1$. The mixture separates from a randomly perturbed homogeneous state $\overline{u} = 0.4$. The mesh is composed of 256^2 control points. The parameters are $\varepsilon^2 = 10^{-3}$ and $\delta = 10^{-4}$.

(a) $t = 0.1$ (b) $t = 0.3$
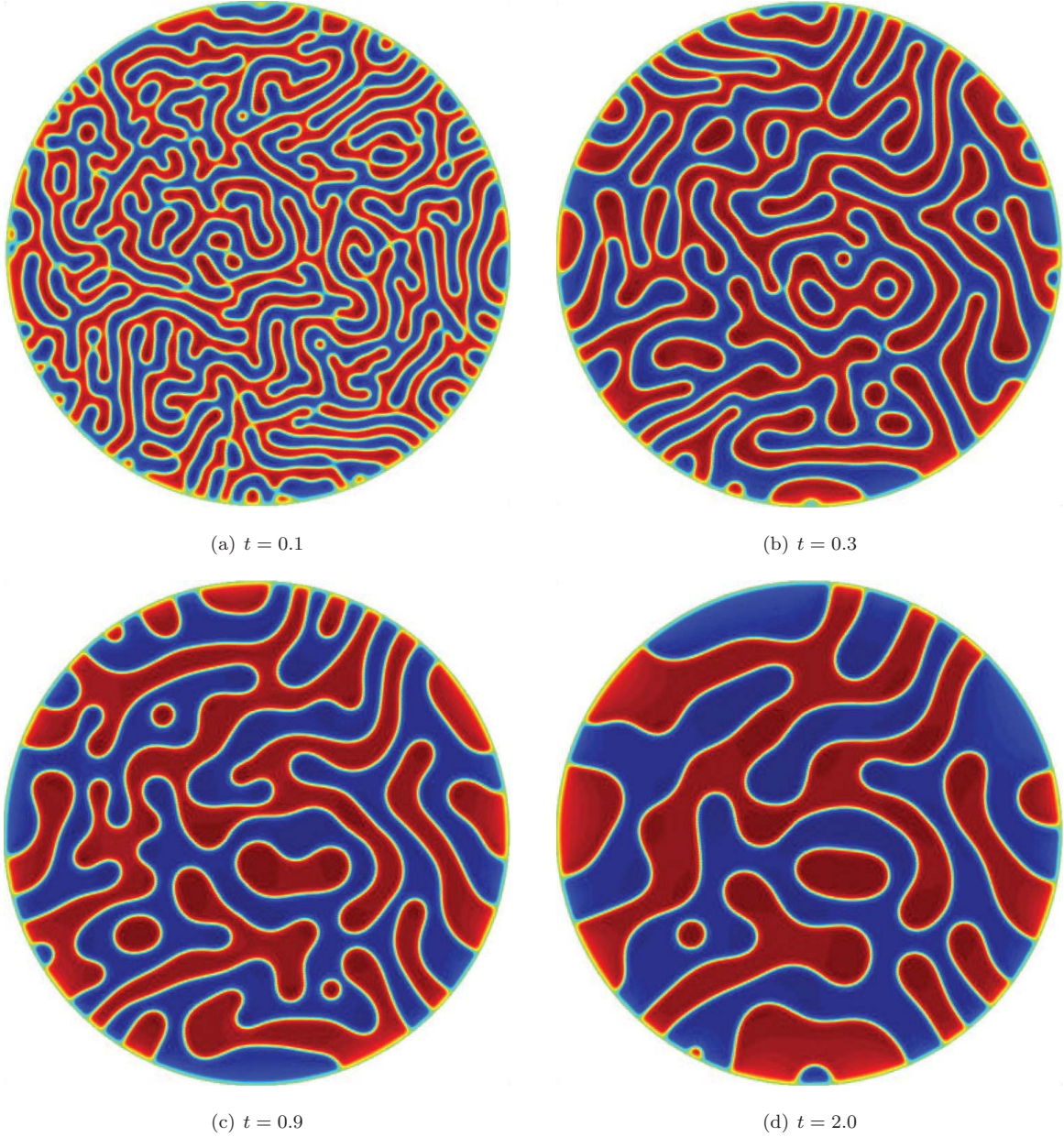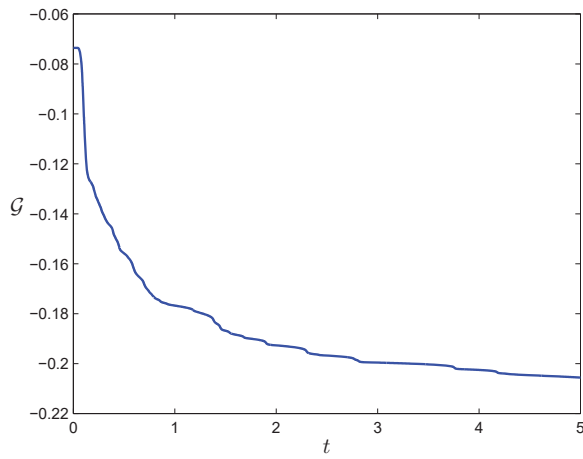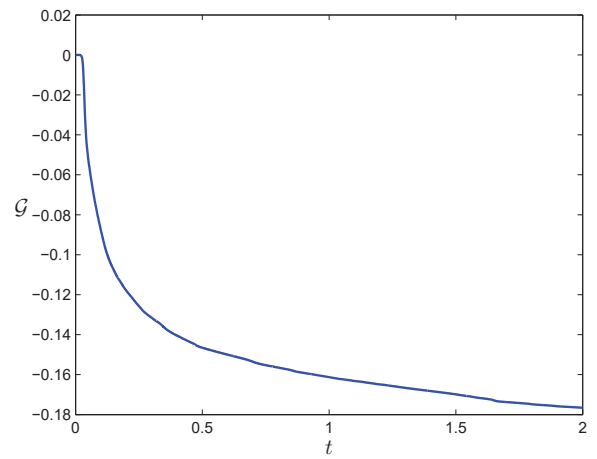
(c) $t = 0.9$ (d) $t = 2.0$

Figure 11: Spinodal decomposition on a circle of radius $r = 4$. We use homogeneous Dirichlet boundary conditions and let the mixture separate from a randomly perturbed uniform solution $\overline{u} = 0$. The computational mesh is composed of 256^2 control points and the time step is $\delta = 10^{-4}$. The interface length scale is given by $\varepsilon^2 = 10^{-3}$.

(a) Spinodal decomposition on an annulus

(b) Nucleation on a circle

Figure 12: Time evolution of the free energy for the numerical examples on mapped domains. We observe that the free energy is monotonically decreasing in both cases. We note, however, that for the example with Dirichlet boundary conditions, the free energy does not necessarily have to decrease.